



Adaptive shrinking reconstruction framework for cone-beam X-ray luminescence computed tomography

HAIBO ZHANG,¹  XIAODONG HUANG,² MINGQUAN ZHOU,¹ 
GUOHUA GENG,¹ AND XIAOWEI HE¹

¹School of Information Sciences and Technology, Northwest University, Xi'an, Shannxi 710027, China

²Baoji Central Hospital, Baoji, Shannxi 710127, China

*zhanghb@nwu.edu.cn

Abstract: Cone-beam X-ray luminescence computed tomography (CB-XLCT) emerged as a novel hybrid technique for early detection of small tumors *in vivo*. However, severe ill-posedness is still a challenge for CB-XLCT imaging. In this study, an adaptive shrinking reconstruction framework without *a priori* information is proposed for CB-XLCT. In reconstruction processing, the mesh nodes are automatically selected with higher probability to contribute to the distribution of target for imaging. Specially, an adaptive shrinking function is designed to automatically control the permissible source region at a multi-scale rate. Both 3D digital mouse and *in vivo* experiments were carried out to test the performance of our method. The results indicate that the proposed framework can dramatically improve the imaging quality of CB-XLCT.

© 2020 Optical Society of America under the terms of the [OSA Open Access Publishing Agreement](#)

1. Introduction

As a novel hybrid X-ray CT/molecular imaging modality, X-ray luminescence computed tomography (XLCT) can be used for drug research, metabolic research and clinical diagnosis [1–3]. Compared with conventional optical molecular modalities, i.e. fluorescence molecular tomography (FMT) [4] and bioluminescence tomography (BLT) [5], XLCT has been shown to be able to avoid obvious background noise while imaging deep tissue. Furthermore, XLCT has been used in small animals *in vivo* [6–8].

In general, narrow-beam XLCT, pencil-beam XLCT (PB-XLCT) [9], and cone-beam XLCT (CB-XLCT) [1–3] are three main types of common XLCT. Xing *et al.*, firstly proposed a narrow-beam XLCT to realize the 3D reconstruction of nanoparticles [2]. Further, using a collimated pencil-beam X-ray, Li *et al.*, designed a pencil-beam XLCT to recover the deep targets [9]. Besides, narrow beam XLCT was proposed based on a limited-view imaging technique [10]. However, although the above two XLCT techniques have high spatial resolution, long data acquisition time significantly limits their application in drug research and early tumor detection [11]. To resolve the problem, Chen *et al.*, proposed a cone-beam XLCT (CB-XLCT) imaging system, which can sharply reduce the imaging time and improve the X-ray dose utilization efficiency [12].

Directly caused by the insufficiency of external measurements, high ill-posedness is still a technical bottleneck for XLCT [3]. Extensive researches have been conducted to improve reconstruction results. Chen *et al.*, used the multi-spectral data to realize quantitative reconstruction [13]. Liu *et al.*, proposed a single-view reconstruction by a wavelet transform method [14]. Gao *et al.*, presented a truncated singular value decomposition (TSVD) approach for CB-XLCT imaging [7]. Generally, *a priori* information, such as structural prior, optical properties, sparsity of target distribution and permissible source region (PSR) can effectively improve reconstruction results [15–19].

The PSR method can reduce the scale of inverse problem by reducing the number of unknown variables, and has been widely employed to BLT, FMT and XLCT [13,20–24]. However, the permissible region (PR) is traditionally determined by a rough and subjective estimation from the surface photon distribution [13]. When the light source is deep in imaging body, the accuracy of the method is affected [25]. Although the iterative estimation can be adopted to improve the above deficiency, the threshold for the selection of PR is usually a fixed manually set rate, leading to excessive iterations and high computational cost [26]. To overcome this obstacle, we developed an adaptive shrinking permissible source region (ADS_PSR) framework for the imaging of small targets without *a priori* information in this study. Meanwhile, a multi-scale kernel function is designed to accelerate the shrinking rate automatically. To the best of our knowledge, this is the first time that a special PSR framework was proposed to alleviate the ill-posedness of inverse problem for CB-XLCT imaging. Several numerical simulation experiments and an *in vivo* experiment have been performed to validate the effectiveness and robustness of the proposed framework.

The contributions of the paper can be summarized as follows: 1) a novel PSR framework was proposed to alleviate the ill-posedness of inverse problem of CB-XLCT; 2) instead of the traditionally manual experience, a new shrinking function was designed to automatically obtain permissible region; and 3) the proposed framework is suitable for combining with mainstream reconstruction algorithms for CB-XLCT.

In Section 2, the imaging model of CB-XLCT and the proposed ADS_PSR framework are introduced. Then, numerical simulation experiments and the *in vivo* experiment are demonstrated in Section 3. Finally, we discuss the results and draw a conclusion in Section 4.

2. Method

2.1. Imaging system of the CB-XLCT

As illustrated in Fig. 1, the traditional scheme diagram of CB-XLCT imaging system mainly includes the following parts: a cone beam X-ray source to achieve X-ray excitation, a CMOS X-ray detector panel to collect X-ray projection data, an electron-multiplying CCD (EMCCD) camera to collect luminescent data for optical imaging, and a rotation stage to realize multi-angles X-ray excitation. Hence, X-ray CT imaging and 3D optical imaging can be achieved together by CB-XLCT system.

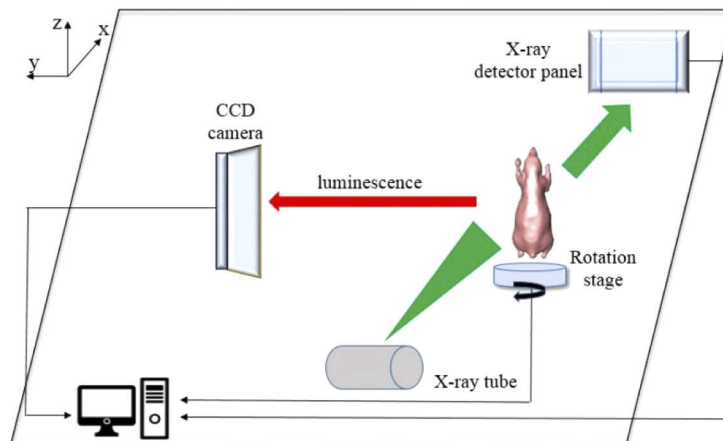


Fig. 1. Schematic diagram of CB-XLCT system [11–12].

2.2. Imaging model of the XLCT

In detail, X-rays are emitted by the cone-beam X-ray source and traveled through biological tissues. Based on Beer-Lambert's law, the propagation process of X-ray traveled in tissues can be modeled as follows [11]:

$$X(r) = X_0 \exp\left\{-\int_{r_0}^r \mu_x(\tau) d\tau\right\} \quad (1)$$

where $X(r)$ is the X-ray intensity at position r in tissue, X_0 is the initial X-ray intensity at r_0 , and μ_x is the X-ray attenuation coefficient which can be calculated via an attenuation-based CT technique [1].

Sequentially, once nanoparticles distributed in the imaging object are irradiated by X-rays, the visible or NIR light will be emitted. This emission light can be expressed as the following linear relationship:

$$S(r) = \varepsilon X(r) \rho(r) \quad (2)$$

where $S(r)$ is the target, which is often used to mimic the small tumor. $\rho(r)$ is the nanophosphor concentration at position r , and ε is the light yield of nanoparticles.

Due to the highly scattering and weakly absorbing properties of light in biological tissues, the visible or near infrared (NIR) light transmitted in the tissues can be modeled by the following diffusion equation (DE) model with the Robin boundary condition as follows [27–28]:

$$\begin{cases} -\nabla[D(r)\nabla\Phi(r)] + \mu_a(r)\Phi(r) = S(r) & r \in \Omega \\ \Phi(r) + 2\kappa D(r)[\nu\nabla\Phi(r)] = 0 & r \in \partial\Omega \end{cases} \quad (3)$$

where $D(r) = (3(\mu_a(r) + \mu'_s(r)))^{-1}$ is the diffusion coefficient, where $\mu_a(r)$ and $\mu'_s(r)$ is the absorption and reduced scattering coefficient, respectively. Ω is the domain of the image object and $\partial\Omega$ is the corresponding boundary. $\Phi(r)$ is the photon fluence at position r . ν is the outward unit normal vector to boundary, and κ is a constant describing the optical reflective index mismatch.

Based on the finite-element (FEM) method [29], Eqs. (1) and (3) can be converted into a linear relationship between the unknown nanophosphor distribution ρ and the NIR measurement J as following matrix-form equation:

$$J = A\rho \quad (4)$$

where A is the system matrix which is used to map the unknown ρ to known measurement J [8].

2.3. Reconstruction problem

The goal of CB-XLCT imaging is to recover the unknown distribution of the nanophosphor based on the NIR measurement J captured by the EMCCD camera. However, the high scattering character of light in biological tissue leads to a poorly conditioned system matrix A . Thus, that it is impractical to solve ρ directly from Eq. (4). In addition, the usually limited optical measurements and other experiment conditions further increase the difficulty of solution to the above inverse problem. The distribution of nanophosphors in biological tissue are usually small and sparse, compared to the entire imaging body [12–14]. Herein, the compressed sensing (CS) theory can be applied to solve ρ by converting Eq. (4) into the following optimization problem [30].

$$\min \|A\rho - J\|_2^2 + \tau \|\rho\|_p \quad (5)$$

where τ is the regularization coefficient. $\|\rho\|_p$ is the L_p -norm of ρ . When $p = 0$, Eq. (5) is L_0 norm, which is NP-hard. When $p = 1$, Eq. (5) is the well-known L_1 -norm as the convex relaxation of L_0 -norm, which has been a widely used sparsity-inducing norm for CB-XLCT imaging [13]. When $p = 2$, Eq. (5) is the L_2 -norm, which is the commonly used Tikhonov regularization [31].

2.4. Adaptive shrinking permissible source region framework for CB-XLCT imaging

Generally, the size of system matrix A in Eq. (5) is usually large and this obviously aggravates the ill-posedness of the inverse problem [11,14]. To achieve high imaging quality, ADS_PSR framework has been developed in this study. The implementation of the ADS_PSR framework is started from the entire domain to a small area without *a priori* information. From every shrinking iteration k , the permissible region (PR) R_k is updated by removing nodes with lower recovered density. We define a following vector P_k to reduce the scale of inverse problem:

$$P_k = \begin{cases} 1 & \text{if node } i \text{ is within the permissible region} \\ 0 & \text{otherwise} \end{cases} \quad (6)$$

As soon as P_k is determined, A and ρ in Eq. (5) become $A_k = A_{k-1} \otimes P_k$ and $\rho_k = \rho_{k-1} \otimes P_k$, respectively. \otimes represents the operation that removes columns in previous matrix A_{k-1} with zero-element in column vector P_k . Then, an updated inverse problem has been converted as follows:

$$\min_{R_k} \|A_k \rho_k - J\|_2^2 + \tau_k \|\rho_k\|_p \quad (7)$$

After solving Eq. (7), a new PR is determined by ranking the magnitude of X_k in the decreasing order for next iterative reconstruction.

Aiming to automatically select the group of mesh nodes to obtain a shrinking ρ_k without manual intervention, we designed an adaptive kernel function to automatically speed up the shrinking process at a multi-scale rate as follows:

$$\zeta_k = 1 - \frac{\beta \cdot \exp[-(k-1)/\alpha]}{1 + \beta \cdot \exp[-(k-1)/\alpha]} \quad (8)$$

where k is the iterations which is set from 1. α and β is multi-scale factor and nonnegative coefficient, respectively. α and β are all determined experientially to confine the shrinking rate. For the reconstruction, the range of α and β is [2.5, 3.5] and [3.5, 7.5], respectively. Figure 1 shows the value of ζ function with the increase of k ($\alpha = 3$, $\beta = 6$).

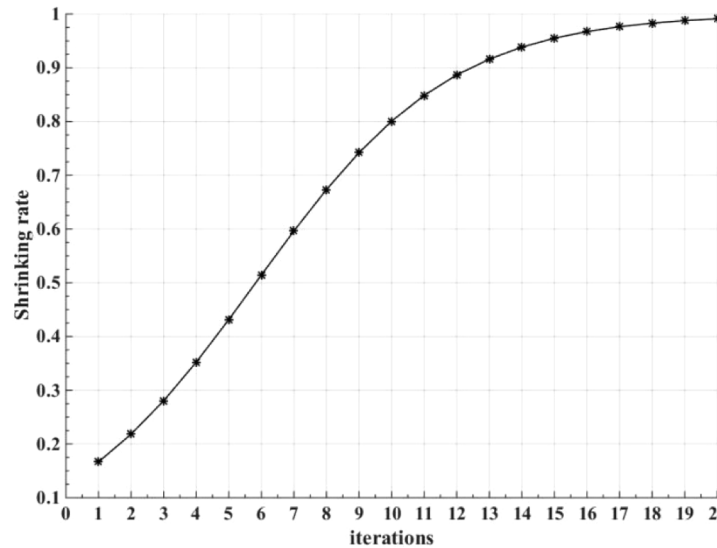


Fig. 2. The multi-scale of ζ function with the increase of k .

In the implementation, $length(R)$ is the number of nodes related to the PR determined in the current iteration. Next, the number of nodes for the next round reconstruction with higher recovered density is automatically obtained by $\lfloor Num(R) \cdot \zeta_k \rfloor$ and $\lfloor \cdot \rfloor$ is the integer operation. With the increase of K , the trend of solution $\rho(R_i)$ gradually to be stable, which means that the difference of number of nodes between the adjacent rounds is gradually reduced. Especially, as can be seen in Fig. 2, about 90% of the nodes of the previous solution ρ_{k-1} will be maintained as the value of k increases to 10, compared with 10% of that at the beginning. Meanwhile, the number of discarded nodes with lower recovered density decrease correspondingly. Consequently, the PR will correspondingly shrink to a stable area and a stable solution ρ can be acquired. Thus, the function ζ_k can adaptively fit this case with a multi-scale rate. Table 1 shows details of the proposed framework for CB-XLCT imaging.

Table 1. Procedure of the adaptive shrinking permissible source region framework for CB-XLCT imaging

Algorithm: ADS_PSR framework for CB-XLCT imaging

Step 1: Parameter initialization. Set the iteration number $k = 1$ and compute the multi-scale rate ζ as in Eq. (8) if $k > 1$. Set the final nodes $N_f = 10$ according to experience.

Step 2: Solving Eq. (5) for Global reconstruction to determine a current PR.

Step 3: Sort recovered density of current nodes in the decreasing order, choose $\lfloor Num(R) \cdot \zeta_k \rfloor$ mesh nodes with higher recovered density to form a new PR.

Step 4: Get the vector P_k by Eq. (6) and Computing the optimized system matrix A_k .

Step 5: Local reconstruction based on Eq. (7) to refine a solution.

Step 6: if $\sum |A_{k+1}\rho_{k+1} - A_k\rho_k| / |A_k\rho_k| \leq \xi$ or the number of nodes of refined PR $N_{k+1} \leq N_f$, output the solution ρ based on the final PSR and quit; otherwise, go to step 2 for next round iteration.

3. Experiments and results

In this section, several numerical simulation experiments and an *in vivo* experiment were investigated to evaluate the performance of the proposed framework. For detailed comparison, the traditional iterative shrinking permissible region (ISPR) method was used in our study [19–23]. Besides, some widely-used algorithms in CB-XLCT, including the algebraic reconstruction technique (ART) [32], the incomplete variables truncated conjugate gradient method for sparse L_1 -norm minimization (IVTCG) [33] and the Tikhonov regularization algorithm for L_2 -norm minimization [34] were adopted. Considering that L_1 -norm has been proved efficient for the sparsity-inducing norm for detecting the sparsely distributed tumors [1–3], only our proposed framework and ISPR method incorporate IVTCG algorithm. The threshold value of ISPR was set as 50% and 70% according to previous works [22–23]. In addition, the regularization coefficient τ of IVTCG and Tikhonov is automatically selected by the L-curve method [35–36]. The multi-scale factor α and nonnegative coefficient β of ζ_k function were set empirically as 3 and 5, respectively.

Several quantitative indexes, such as absolute location error (LE) [11], recovered density (RD) [13], relative quantity error (RQE) [13] and the percentage of non-zero coefficient (PNZ) [37] were adopted for assessment. The experiment codes were written in MATLAB and was performed on a desktop computer with 2.20 GHz Intel Xeon Processor I7-4702MQ and 16G RAM.

3.1. Numerical simulation experiments

A mouse atlas of CT data, as demonstrated in Fig. 3(a), with a single nanophosphor target and double nanophosphor targets respectively was adopted to test our method. The single nanophosphor target was located with center of (17.8, 6.6, 50.8) mm. The double nanophosphor

targets were located with center of (11.2, 14.6, 60) mm and (22.8, 14.6, 60) mm. The 2D views of CT slices of the digital mouse model with single-target and double-targets were shown in Fig. 3(d) and Fig. 3(e), respectively. All targets were designed as a small ball with a radius of 1 mm to mimic small tumor. The voltage and current of X-ray source were set as 50kVp voltage and 1 mA, respectively. The attenuation coefficient of X-ray was set as 0.0535 mm^{-1} [38]. The homogeneous absorption coefficient and reduced scattering coefficient of the two digital mouse models were set as 0.3 mm^{-1} and 10 mm^{-1} , respectively [39]. The concentration of all targets was $0.3183 \mu\text{g}/\text{mm}^3$, and the corresponding light yield were $0.15 \text{ cm}^3/\text{mg}$ [12].

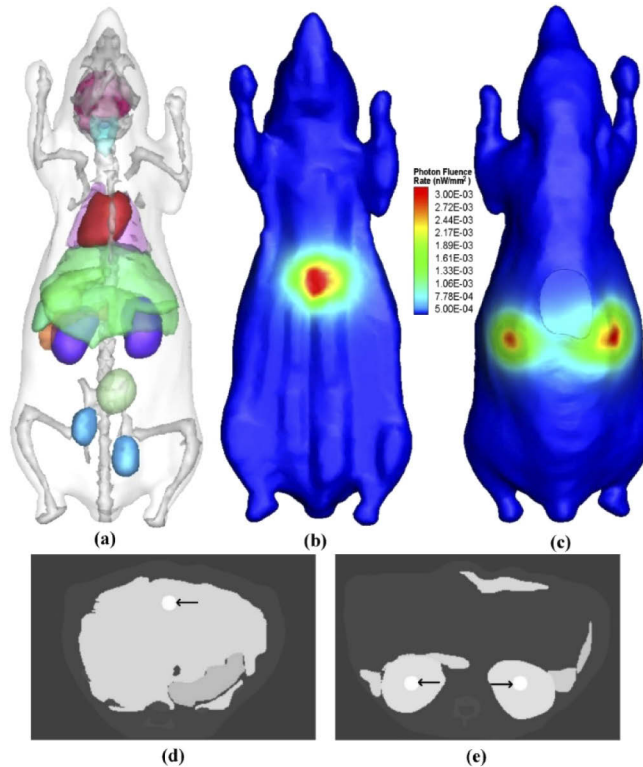


Fig. 3. Reconstruction model in simulation experiment. (a) 3D Mouse Model (b) Forward simulation of single-target case (c) Forward simulation of double-targets case (d) 2D view of CT slice for the single-target case (e) 2D view of CT slice for the double-targets case.

The digital mouse model for single-target case was discretized into 47733 nodes and 251509 tetrahedral elements. The digital mouse model for double-targets case was discretized into 47656 nodes and 251161 tetrahedral elements. A cone beam X-ray source was used to excite the two digital mouse models with every 20 deg intervals during a 360-deg scan. By using the Monte Carlo (MC) method, which is implemented by the Chinese Academy of Sciences Molecular Optical Simulation Environment (MOSE) software [40], we could get the forward simulation results for the single-target case and the double-targets case as demonstrated in Fig. 3(b) and Fig. 3(c), respectively.

3.1.1. Single-target experiment

For the single-target case, a mesh with 6367 nodes and 32158 tetrahedral elements (average mesh size of about 0.41 mm) was used for the inverse reconstruction. The 2D views of the recovered results at $Z = 50.8 \text{ mm}$ plane by ADS_PSR + IVTCG, IPSR with artificial threshold

50% + IVTCG, IPSR with artificial threshold 70% + IVTCG, IVTCG with no processing, Tikhonhov with no processing and ART with no processing are shown in Fig. 4, where the real position of nanophosphor target is marked as the red circle. Table 2 presents the corresponding quantitative results.

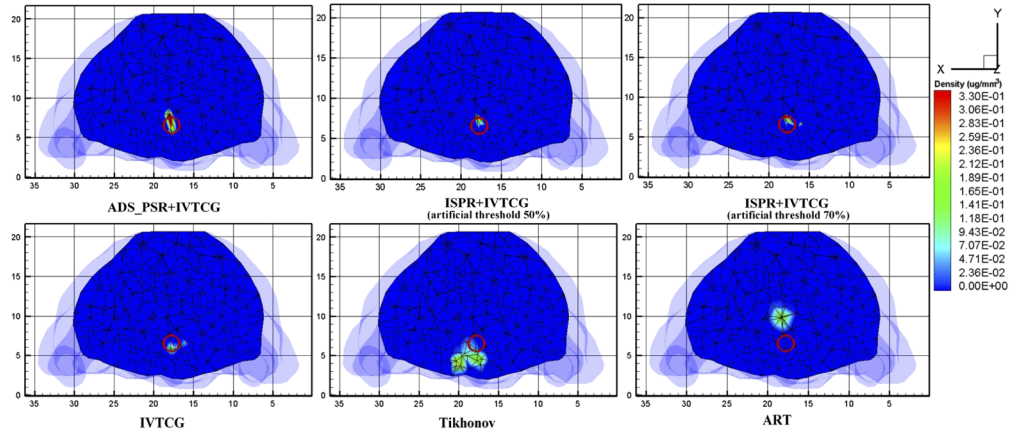


Fig. 4. The 2D views ($Z = 50.8$ mm plane) of the reconstructed results for the single-target reconstruction.

Table 2. Quantitative results of the single-target case

Algorithm	Location error (mm)	Recovered density ($\mu\text{g}/\text{mm}^3$)	Relative quantity error (%)	PNZ (%)	Iteration number
ADS_PSR + IVTCG	0.53	0.29	9.29	1.22	6
IPSR + IVTCG (artificial threshold 50%)	0.83	0.27	14.36	2.76	11
IPSR + IVTCG (artificial threshold 70%)	0.89	0.27	14.36	2.74	20
IVTCG	1.04	0.26	16.22	3.05	\
Tikhonhov	2.09	0.19	40.04	8.43	\
ART	3.68	0.12	62.64	11.52	\

From Fig. 4 and Table 2, it is significant that ADS_PSR and IPSR outperform the traditional algorithms. The ADS_PSR method with IVTCG achieves the least LE and RQE, the highest RD. However, with no processing, the LE of IVTCG is larger than 1 mm, which means the improvement of reconstruction by the proposed framework is remarkable. Furthermore, the PNZ of the ADS_PSR method with IVTCG is the lowest, denoting that the solution of our proposed method is the sparsest. As shown in Fig. 5, the iteration number of ADS_PSR is significantly less than that of IPSR with artificial threshold.

3.1.2. Double-targets case

In the double-targets simulation experiment, a mesh with 6746 nodes and 35189 tetrahedral elements (average mesh size of about 0.38 mm) was adopted. Figure 6 gives the 2D views of the recovered results at $Z = 60$ mm plane by ADS_PSR + IVTCG, IPSR with artificial threshold 50% + IVTCG, IPSR with artificial threshold 70% + IVTCG, IVTCG with no processing, Tikhonhov with no processing and ART with no processing. Table 3 presents the corresponding

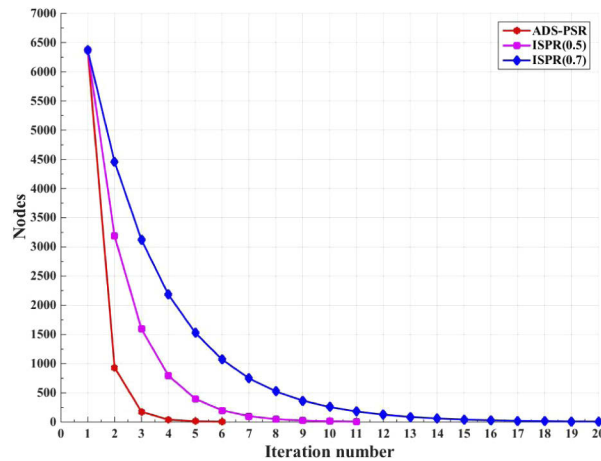


Fig. 5. The iteration number of ADS_PSR and ISPR with artificial threshold in single-target case.

results and Fig. 7 is the iteration number of ADS_PSR and ISPR with artificial threshold in double-targets case.

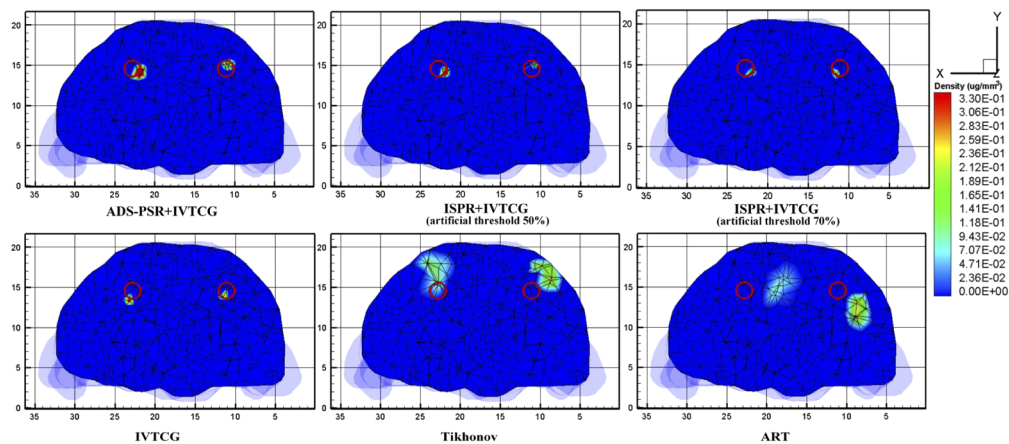


Fig. 6. 2D views ($Z = 60$ mm plane) of the reconstructed results for the double-targets reconstruction.

As can be seen in Figs. 6–7, and Table 3, all methods can separate the two targets. The proposed ADS_PSR with IVTCG yields the best results. However, the LE of one target are larger than 1 mm by ISPR method and IVTCG algorithm. Besides, the results of Tikhonov with no processing and ART with no processing are similar to that of single target reconstruction.

3.1.3. Stability analysis with single-target reconstruction

To further assess the stability and robustness of the proposed method for CB-XLCT imaging, we conduct a series of experiments to investigate the reconstructed results in this section. Specifically, the influence of nodes and tetrahedral elements, the influence of measurements, and the influence of the measurement with different noise level were all evaluated with single-target reconstruction.

In the previous experiments, the surface data of the phantom were obtained with 20° intervals for reconstruction. The reduction in measurement data due to decreased view angles will directly

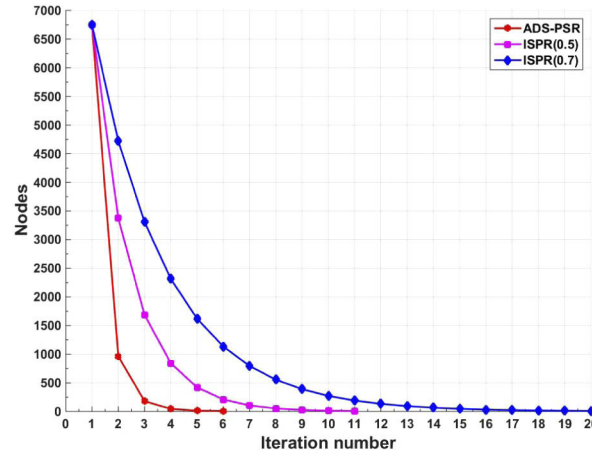


Fig. 7. The iteration number of ADS_PSR and ISPR with artificial threshold in double-targets case.

Table 3. Quantitative results of the double-targets case

Algorithm	Location error (mm)		Recovered density ($\mu\text{g}/\text{mm}^3$)		Relative quantity error (%)		PNZ (%)	Iteration number
	Target 1	Target 2	Target 1	Target 2	Target 1	Target 2		
ADS_PSR + IVTCG	0.86	0.57	0.27	0.25	14.36	20.89	2.93	6
ISPR + IVTCG (artificial threshold 50%)	1.09	0.63	0.25	0.21	20.89	32.37	3.37	11
ISPR + IVTCG (artificial threshold 70%)	1.20	0.63	0.21	0.20	32.37	36.53	3.51	20
IVTCG	1.21	0.67	0.20	0.21	36.53	32.37	3.66	\
Tikhonhov	2.69	2.91	0.19	0.18	38.86	41.67	9.11	\
ART	4.35	3.55	0.11	0.18	64.35	41.67	15.83	\

aggravate the ill-posed inverse problem and thus affect the reconstruction. Thus, the influence of different view numbers on the proposed method was investigated firstly. We gradually reduced the number of view numbers to 12, 9, 6, and 3. The corresponding quantitative results were reported in Table 4, and Fig. 8 gives the graph results on LE and RD. As shown Fig. 8, although the quality of the proposed is influenced with the reducing of view angles, the LE are all below 0.7 mm. Meanwhile, the value of RD decreased correspondingly. But the value of RD is almost above $0.2 \mu\text{g}/\text{mm}^3$. Herein, it is obvious that the proposed method is robust in different view angles.

Table 4. Comparison results for reconstruction single-target by ADS_PSR + IVTCG with different measurements

The number of view angles	Location error (mm)	Recovered density ($\mu\text{g}/\text{mm}^3$)	Relative quantity error (%)
12	0.40	0.27	14.00
9	0.40	0.26	14.40
6	0.41	0.21	34.08
3	0.65	0.14	54.90

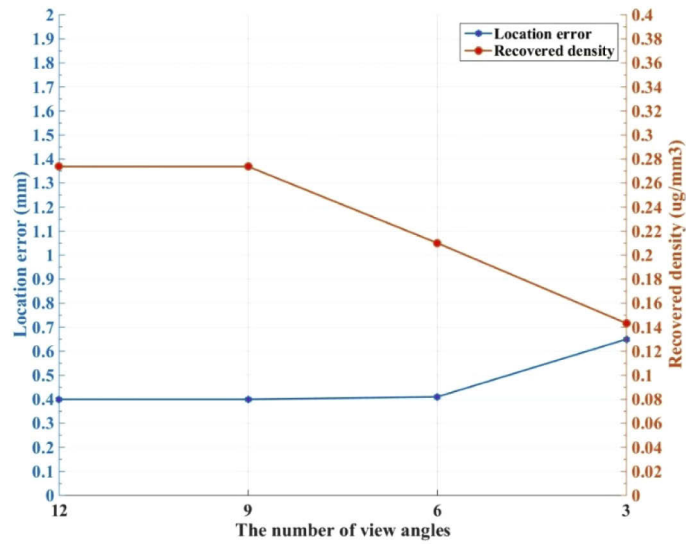


Fig. 8. Illustration of LE and RD at different number of view angles

It is noted that noise was unavoidable in CB-XLCT imaging [1–3], a group of experiments with noise were also performed. Concretely, Gaussian noise with five different noise levels (5%, 10%, 15%, 20% and 25%) was added to the measurement data of single-target reconstruction. Table 5 and Fig. 9 show the corresponding reconstruction results. Obviously, the LE are all around (even below) 0.5 mm. The RD are all above $0.2 \mu\text{g}/\text{mm}^3$. It is clear that the proposed method is robust to measurement noise.

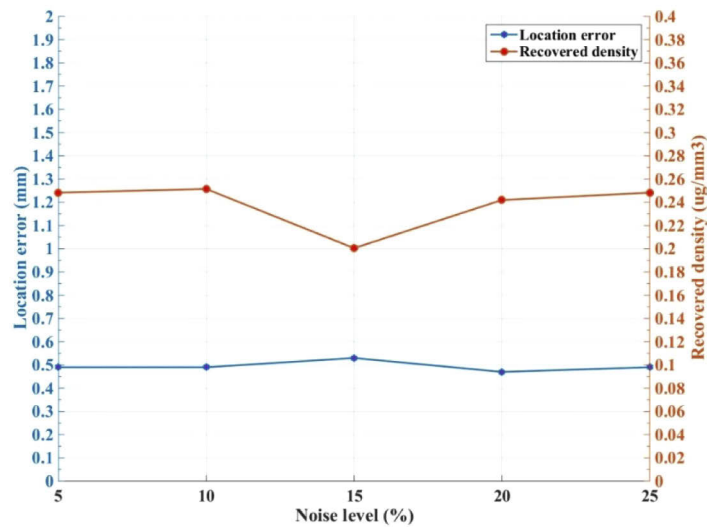


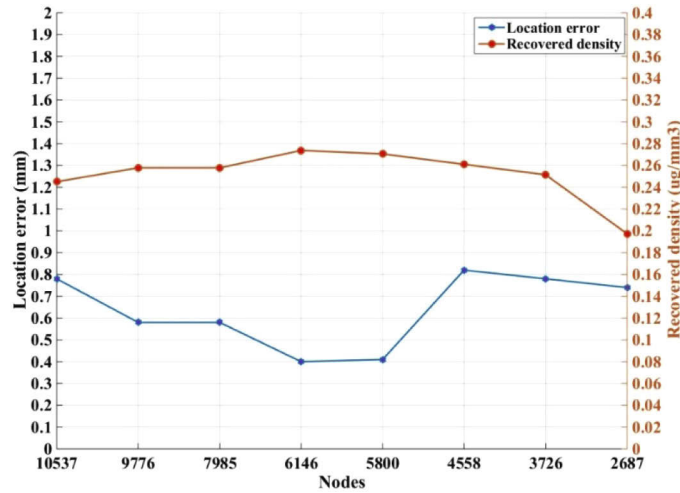
Fig. 9. Illustration of LE and RD at different noise levels.

To further evaluate the stability of the proposed method, the influence of nodes and tetrahedral elements are investigated. Commonly used different level numbers of nodes and tetrahedral elements (from around 10000 nodes to 2000 nodes) were adopted for reconstruction. The detailed quantitative results are shown in Table 6 and Fig. 10. We found that although the numbers of

Table 5. Comparison results for the reconstruction single-target by ADS_PSR + IVTCG with different noise levels

Noise level (%)	Location error (mm)	Recovered density ($\mu\text{g}/\text{mm}^3$)	Relative quantity error (%)
5	0.49	0.25	21.53
10	0.49	0.25	21.53
15	0.53	0.20	36.59
20	0.47	0.24	24.32
25	0.49	0.25	21.53

nodes decreases from 10635 to 2593, the LE changes basically between 0.4 and 0.8. Specially, the number of nodes from 5000 to 6000 give the best results on LE. Similar to the results of previous experiment with noise, the RD with different numbers of nodes and tetrahedral elements are all above $0.2 \mu\text{g}/\text{mm}^3$.

**Fig. 10.** Illustration of LE and RD at different number of nodes.**Table 6. Comparison results for the reconstruction single-target by ADS_PSR + IVTCG with different numbers of nodes and tetrahedral elements**

Nodes	Tetrahedral elements	Mesh size (mm)	Location error (mm)	Recovered density ($\mu\text{g}/\text{mm}^3$)	Relative quantity error (%)
10635	51973	about 0.26	0.78	0.25	23.02
9734	47165	about 0.28	0.58	0.26	19.37
7685	36782	about 0.36	0.58	0.26	19.29
6146	31988	about 0.42	0.40	0.27	14.00
5800	27138	about 0.49	0.41	0.27	15.02
4558	20938	about 0.63	0.82	0.26	18.03
3720	16836	about 0.79	0.78	0.25	21.12
2593	11345	about 1.17	0.74	0.20	37.75

3.2. *In vivo* experiment

To ensure the feasibility of our proposed method in *in vivo* applications of CB-XLCT, a female eight-week-old mouse was used for the *in vivo* experimental [14]. The homogeneous absorption coefficient and reduced scattering coefficient of *in vivo* data were set to be 0.3 mm^{-1} and 10 mm^{-1} , respectively [39]. The voltage and current of a cone-beam X-ray source (Apogee, Oxford Instruments, USA) with a micro 55-mm f/2.8 lens (Nikkor, Nikon, Japan) were set to be 50 KVP and 1 mA, respectively. A highly sensitive CCD camera (PIXIS 2048, Princeton Instruments, USA) with a micro 55-mm f/2.8 lens (Nikkor, Nikon, Japan) was mounted vertical to the X-ray axis to capture the optical data (620 nm). The integrating time and binning of the CCD were set to be 30 s and 2×2 , respectively. For the optical imaging, the 360 deg luminescent photons data acquired by the CCD with 45 deg intervals was adopted for the inverse reconstruction. Meanwhile, a flat-panel detector (C7921CA-02, Hamamatsu, Japan) was used to fulfill the 360 deg micro-CT imaging with 1 deg intervals. The micro-CT imaging was performed via the Feldkamp-Davis-Kress (FDK) method [41]. The micro-CT result of the female mouse is demonstrated in Fig. 11.

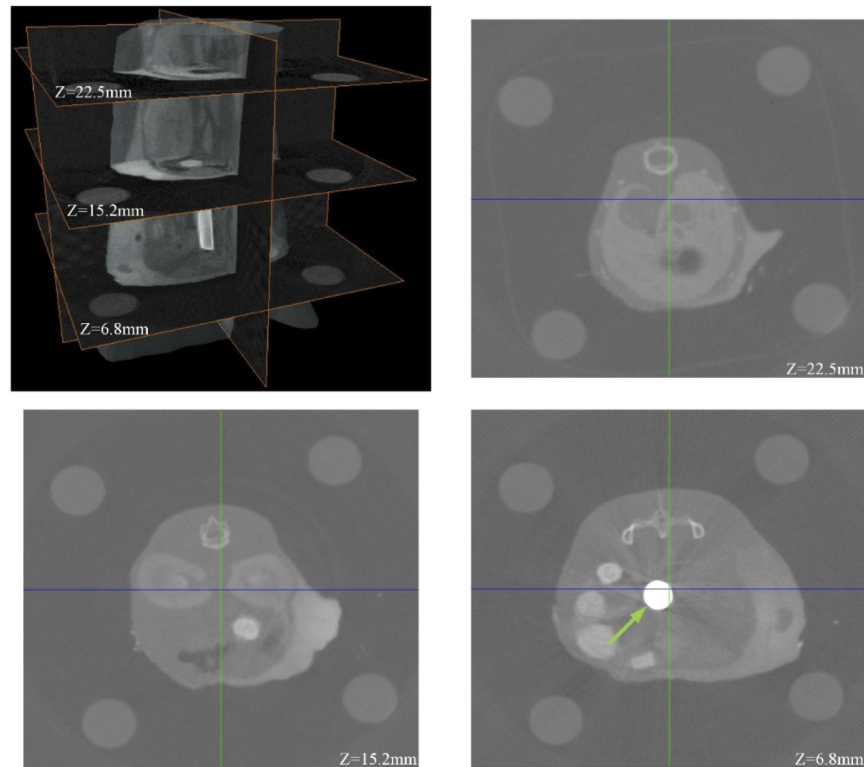
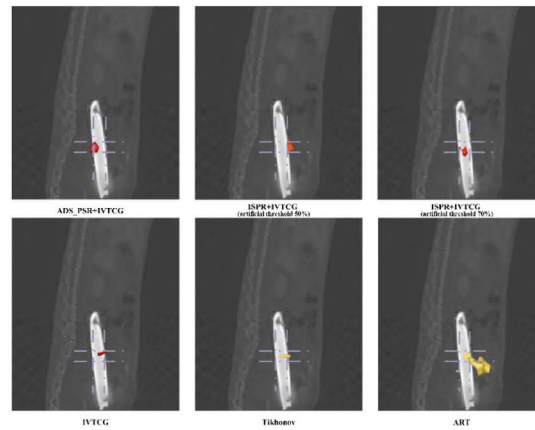
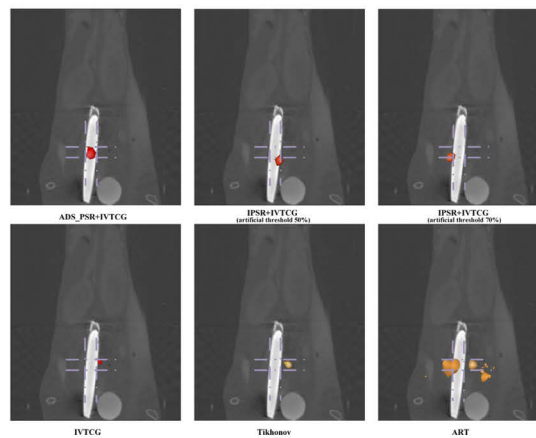


Fig. 11. The micro-CT result of the female mouse.

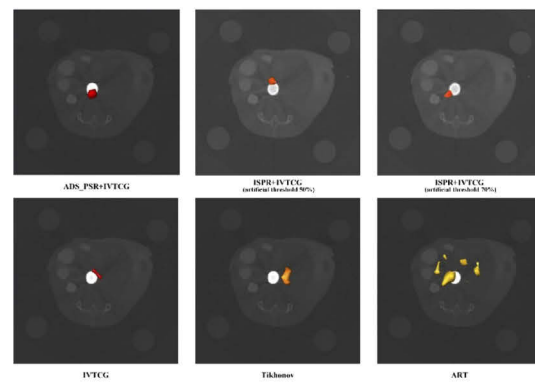
According to the result of stability analysis, the mesh with 5987 nodes and 28816 tetrahedral elements (average mesh size of about 0.46 mm) was utilized in *in vivo* experiment for inverse reconstruction. The reconstruction results overlaid with CT data are shown in Fig. 12. The detailed information of results are listed in Table 7. Figure 13 is the iteration number of ADS_PSR and ISPR with artificial threshold. As we can see from Fig. 12 and Table 7, the quantitative result of the proposed method is satisfactory for *in vivo* experiment, where the LE is less than 1 mm.



(a)



(b)



(c)

Fig. 12. Reconstruction results overlaid with CT data of *in vivo* experiment. (a) coronal-view results at $X = 12$ mm. (b) sagittal-view results at $Y = 13.2$ mm; (c) transversal-view results at $Z = 6.8$ mm.

Among all comparison methods, the proposed method yields the sparsest solution. Moreover, the solution of L_2 -norm is not sparse, and the ART fails to obtain feasible reconstruction results.

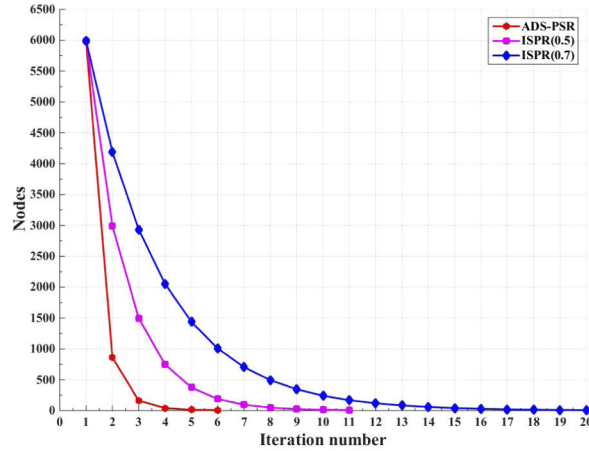


Fig. 13. The iteration number of ADS_PSR and ISPR with artificial threshold of *in vivo* experiment.

Table 7. Quantitative results of the *in vivo* experiment

Algorithm	Location error (mm)	Recovered density (g/cm^3)	Relative quantity error (%)	PNZ (%)	Iteration number
ADS_PSR + IVTCG	0.79	0.013	13.33	2.03	6
ISPR + IVTCG (artificial threshold 50%)	1.13	0.011	25.21	2.56	11
ISPR + IVTCG (artificial threshold 70%)	1.15	0.011	25.21	2.59	20
IVTCG	1.402	0.009	26.67	2.71	\
Tikhonhov	2.186	0.005	53.33	9.08	\
ART	3.945	0.003	60.00	14.27	\

4. Discussion and conclusions

In this study, we proposed an adaptive shrinking permissible source region framework, named ADS_PSR for the recovered result of CB-XLCT imaging. In this framework, the shrinking for reconstruction is beginning from the whole body without *a priori* information. Meanwhile, an adaptive multi-scale kernel function is designed to accelerate the shrinking processing. Specially, in each iteration, the kernel function can automatically select the nodes for next round reconstruction, at a multi-scale rate according to the shrinking process. Thus, a feasible solution by the ADS_PSR can be obtained only with a few mesh nodes. Simulation experiment and *in vivo* experiment were applied to test the performance of the proposed ADS_PSR framework. The widely-used ISPR method, IVTVG, Tikhonov and ART algorithms were employed for comparison. The results demonstrate that all the LE of the simulation case and *in vivo* case by the proposed framework were all less than 1 mm, and corresponding RQE were almost below 20%. Compared with traditional ISPR method with artificial threshold, our proposed method gets more sparse solution with the fewer iterations. These illustrate the potential of the proposed framework

in improving CB-XLCT imaging for feasible and effective reconstruction. Meanwhile, the results of stability case further demonstrated the robustness of the proposed framework for CB-XLCT imaging. Furthermore, the proposed framework can also be extended to other optical molecular modalities, such as FMT and BLT.

However, it should be noted that the size and shape of nanophosphor target cannot be accurately recovered in this paper. Besides, the selection of different number of nodes for reconstruction are often based on experience. Thus, we will focus on these challenges and conduct further research. In conclusion, the proposed framework has a better performance in terms of accuracy, stability and practicability. We hope the proposed framework can facilitate the development of CB-XLCT, as well as other optical molecular tomography technologies.

Funding

National Natural Science Foundation of China (61902317); Science and Technology Plan Program in Shaanxi Province of China (2019JQ-166).

Acknowledgements

The authors would like to thank the School of Life Science and Technology of Xidian University for providing experimental data acquisition system.

Disclosures

The authors declare no conflicts of interest.

References

1. G. Pratz, C. M. Carpenter, C. Sun, and L. Xing, "X-ray luminescence computed tomography via selective excitation: a feasibility study," *IEEE T. Med. Imaging* **29**(12), 1992–1999 (2010).
2. G. Pratz, C. M. Carpenter, C. Sun, R. P. Rao, and L. Xing, "Tomographic molecular imaging of x-ray-excitable nanoparticles," *Opt. Lett.* **35**(20), 3345–3347 (2010).
3. M. Ahmad, G. Pratz, M. Bazalova, and L. Xing, "X-ray luminescence and x-ray fluorescence computed tomography: new molecular imaging modalities," *IEEE Access* **2**(2), 1051–1061 (2014).
4. S. Zhang, X. Ma, Y. Wang, M. Wu, H. Meng, W. Chai, X. Wang, S. Wei, and J. Tian, "Robust reconstruction of fluorescence molecular tomography based on sparsity adaptive correntropy matching pursuit method for stem cell distribution," *IEEE T. Med. Imaging* **37**(10), 2176–2184 (2018).
5. H. Guo, J. Yu, Z. Hu, H. Yi, Y. Hou, and X. He, "A hybrid clustering algorithm for multiple-source resolving in bioluminescence tomography," *J. Biophotonics* **11**(4), e201700056 (2018).
6. X. Liu, Q. Liao, and H. Wang, "In vivo x-ray luminescence tomographic imaging with single-view data," *Opt. Lett.* **38**(22), 4530–4533 (2013).
7. P. Gao, J. Rong, H. Pu, T. Liu, W. Zhang, X. Zhang, and H. Lu, "Sparse view cone beam x-ray luminescence tomography based on truncated singular value decomposition," *Opt. Express* **26**(18), 23233–23250 (2018).
8. G. Zhang, F. Liu, J. Liu, J. Luo, Y. Xie, J. Bai, and L. Xing, "Cone beam x-ray luminescence computed tomography based on bayesian method," *IEEE T. Med. Imaging* **36**(1), 225–235 (2017).
9. C. Li, K. Di, J. Bec, and S. R. Cherry, "X-ray luminescence optical tomography imaging: experimental studies," *Opt. Lett.* **38**(13), 2339–2341 (2013).
10. C. M. Carpenter, G. Pratz, C. Sun, and L. Xing, "Limited-angle x-ray luminescence tomography: methodology and feasibility study," *Phys. Med. Biol.* **56**(12), 3487–3502 (2011).
11. X. Liu, Q. Liao, and H. Wang, "Fast x-ray luminescence computed tomography imaging," *IEEE Trans. Biomed. Eng.* **61**(6), 1621–1627 (2014).
12. D. Chen, S. Zhu, H. Yi, X. Zhang, D. Chen, J. Liang, and J. Tian, "Cone beam x-ray luminescence computed tomography: a feasibility study," *Med. Phys.* **40**(3), 031111 (2013).
13. D. Chen, S. Zhu, X. Chen, T. Chao, X. Cao, F. Zhao, L. Huang, and J. Liang, "Quantitative cone beam x-ray luminescence tomography/x-ray computed tomography imaging," *Appl. Phys. Lett.* **105**(19), 191104 (2014).
14. X. Liu, H. Wang, M. Xu, S. Nie, and H. Lu, "A wavelet-based single-view reconstruction approach for cone beam x-ray luminescence tomography imaging," *Biomed. Opt. Express* **5**(11), 3848 (2014).
15. Y. Tan and H. Jiang, "Dot guided fluorescence molecular tomography of arbitrarily shaped objects," *Med. Phys.* **35**(12), 5703–5707 (2008).

16. F. Stuker, C. Baltes, K. Dikaïou, D. Vats, L. Carrara, E. Charbon, J. Ripoll, and M. Rudin, "Hybrid small animal imaging system combining magnetic resonance imaging with fluorescence tomography using single photon avalanche diode detectors," *IEEE T. Med. Imaging* **30**(6), 1265–1273 (2011).
17. A. Ale, V. Ermolayev, E. Herzog, C. Cohrs, M. H. Angelis, and V. Ntziachristos, "Fmt-xt: in vivo animal studies with hybrid fluorescence molecular tomography–x-ray computed tomography," *Nat. Methods* **9**(6), 615–620 (2012).
18. J. Zhang, J. Shi, X. Cao, F. Liu, J. Bai, and J. Luo, "Fast reconstruction of fluorescence molecular tomography via a permissible region extraction strategy," *J. Opt. Soc. Am. A* **31**(8), 1886–1894 (2014).
19. M. A. Naser and M. S. Patterson, "Bioluminescence tomography using eigenvectors expansion and iterative solution for the optimized permissible source region," *Biomed. Opt. Express* **2**(11), 3179–3193 (2011).
20. J. Feng, K. Jia, G. Yan, S. Zhu, C. Qin, Y. Lv, and J. Tian, "An optimal permissible source region strategy for multispectral bioluminescence tomography," *Opt. Express* **16**(20), 15640–15654 (2008).
21. X. He, F. Dong, J. Yu, H. Guo, and Y. Hou, "Reconstruction algorithm for fluorescence molecular tomography using sorted L-one penalized estimation," *J. Opt. Soc. Am. A* **32**(11), 1928–1935 (2015).
22. X. Song, D. Wang, N. Chen, J. Bai, and H. Wang, "Reconstruction for free-space fluorescence tomography using a novel hybrid adaptive finite element algorithm," *Opt. Express* **15**(26), 18300–18317 (2007).
23. H. Yi, P. Jiao, X. Li, J. Peng, and X. He, "Three-way decision based reconstruction frame for fluorescence molecular tomography," *J. Opt. Soc. Am. A* **35**(11), 1814–1822 (2018).
24. P. Svenmarker, C. T. Xu, H. Liu, X. Wu, and S. Andersson-Engels, "Multispectral guided fluorescence diffuse optical tomography using upconverting nanoparticles," *Appl. Phys. Lett.* **104**(7), 073703 (2014).
25. C. Darne, Y. Lu, and E. M. Sevick-Muraca, "Small animal fluorescence and bioluminescence tomography: a review of approaches, algorithms and technology update," *Phys. Med. Biol.* **59**(1), R1–R64 (2014).
26. J. Feng, C. Qin, K. Jia, S. Zhu, X. Yang, and J. Tian, "Bioluminescence tomography imaging in vivo: recent advances," *IEEE J. Select. Topics Quantum Electron.* **18**(4), 1394–1402 (2012).
27. A. D. Klose, B. J. Beattie, H. Dehghani, L. Vider, C. Le, V. Ponomarev, and R. Blasberg, "In vivo bioluminescence tomography with a blocking-off finite-difference sp3 method and mri/ct coregistration," *Med. Phys.* **37**(1), 329–338 (2010).
28. A. D. Klose and E. W. Larsen, "Light transport in biological tissue based on the simplified spherical harmonics equations," *J. Comput. Phys.* **220**(1), 441–470 (2006).
29. W. Cong, G. Wang, D. Kumar, Y. Liu, M. Jiang, L. Wang, E. Hoffman, G. McLennan, P. B. McCray, J. Zabner, and A. Cong, "Practical reconstruction method for bioluminescence tomography," *Opt. Express* **13**(18), 6756–6771 (2005).
30. H. Zhang, G. Geng, S. Zhang, K. Li, C. Liu, Y. Hou, and X. He, "Sparse non-convex l_p regularization for cone-beam x-ray luminescence computed tomography," *J. Mod. Opt.* **65**(19), 2220–2230 (2018).
31. M. Chen, H. Su, Y. Zhou, C. Cai, D. Zhang, and J. Luo, "Automatic selection of regularization parameters for dynamic fluorescence molecular tomography: a comparison of l-curve and u-curve methods," *Biomed. Opt. Express* **7**(12), 5021 (2016).
32. G. T. Herman and L. B. Meyer, "Algebraic reconstruction techniques can be made computationally efficient (positron emission tomography application)," *IEEE T. Med. Imaging* **12**(3), 600–609 (1993).
33. X. He, J. Liang, X. Wang, J. Yu, X. Qu, X. Wang, Y. Hou, D. Chen, F. Liu, and J. Tian, "Sparse reconstruction for quantitative bioluminescence tomography based on the incomplete variables truncated conjugate gradient method," *IEEE T. Med. Imaging* **18**(24), 24825–24841 (2010).
34. X. Cao, B. Zhang, X. Wang, F. Liu, K. Luo, and J. Bai, "An adaptive tikhonov regularization method for fluorescence molecular tomography," *Med. Biol. Eng. Comput.* **51**(8), 849–858 (2013).
35. P. C. Hansen and D. P. O'Leary, "The use of the l-curve in the regularization of discrete ill-posed problems," *SIAM J. Sci. Comput.* **14**(6), 1487–1503 (1993).
36. P. C. Hansen, "Analysis of discrete ill-posed problems by means of the l-curve," *SIAM Rev.* **34**(4), 561–580 (1992).
37. X. He, J. Yu, X. Wang, H. Yi, Y. Chen, X. Song, and X. He, "Half thresholding pursuit algorithm for fluorescence molecular tomography," *IEEE Trans. Biomed. Eng.* **66**(5), 1468–1476 (2019).
38. G. Alexandrakis, F. R. Rannou, and A. F. Chatziioannou, "Tomographic bioluminescence imaging by use of a combined optical-pet (opet) system: a computer simulation feasibility study," *Phys. Med. Biol.* **50**(17), 4225–4241 (2005).
39. D. Hyde, R. Schulz, D. Brooks, E. Miller, and V. Ntziachristos, "Performance dependence of hybrid x-ray computed tomography/fluorescence molecular tomography on the optical forward problem," *J. Opt. Soc. Am. A* **26**(4), 919–923 (2009).
40. S. Ren, X. Chen, H. Wang, X. Qu, G. Wang, J. Liang, and J. Tian, "Molecular Optical Simulation Environment (MOSE): A Platform for the Simulation of Light Propagation in Turbid Media," *PLoS One* **8**(4), e61304 (2013).
41. L. A. Feldkamp, L. C. Davis, and J. W. Kress, "Practical cone-beam algorithm," *J. Opt. Soc. Am. A* **1**(6), 612–619 (1984).